PHYSICAL REVIEW C **98**, 054609 (2018)

Near-barrier photofission in ^{232}Th and ^{238}U

J. A. Silano[1,2,3,*] and H. J. Karwowski[2,3]

[1]*Nuclear and Chemical Sciences Division, Lawrence Livermore National Laboratory, Livermore, California 94550, USA*
[2]*Triangle Universities Nuclear Laboratory, Durham, North Carolina 27708, USA*
[3]*Department of Physics and Astronomy, University of North Carolina - Chapel Hill, Chapel Hill, North Carolina 27599, USA*

(Received 11 July 2018; revised manuscript received 27 August 2018; published 19 November 2018)

A study of photofission of ^{232}Th and ^{238}U was performed by using quasimonoenergetic, linearly polarized γ-ray beams from the High Intensity γ-ray Source at Triangle Universities Nuclear Laboratory. The prompt-photofission neutron polarization asymmetries, neutron multiplicities, and the photofission cross sections were measured in the near-barrier energy range of 4.3 to 6.0 MeV. This data set constitutes the lowest energy measurements of those observables to date using quasimonoenergetic photons. Large polarization asymmetries are observed in both nuclei, consistent with the $E1$ excitation as observed by another measurement of this kind made in a higher-energy range. Previous experimental evidence of a deep third minimum in the ^{238}U fission barrier has been identified as an accelerator-induced background.

DOI: 10.1103/PhysRevC.98.054609

I. INTRODUCTION

There has been much progress over the past 80 years in understanding the fission process but a complete model of the fission mechanism has yet to be established. Recent advances in computing power have facilitated the possibility of a comprehensive microscopic description of the fission process. A complete and quantitatively accurate microscopic fission model would significantly impact a number of fission applications which are currently of interest. The physical observables of fission such as the fission cross section, prompt-neutron multiplicity, fragment masses, and angular distributions are determined by the structure of the fission barrier—the potential-energy surface that an excited nucleus must overcome to split apart. In order for any calculation to be able to predict those observables accurately, it must be able to predict the effective fission barrier. The barrier cannot be directly measured and thus can only be inferred through measurements of these fission observables.

Recent experimental [1–4] and theoretical [5–7] results have been in disagreement over the topic of a "third minimum," or third well, in the potential-energy surface (PES) describing the fission barrier of actinides. The barriers are typically presented by projecting the multidimensional PES along the quadrupole deformation of the nucleus, β. The second and third wells are then seen as relative minima in the potential-energy curve of this one-dimensional (1D) model at β values corresponding to spheroidal nuclear shapes with major to minor axis ratios of approximately 2 : 1 and 3 : 1, respectively. Owing to the deformations of the nuclear shapes, states in these potential minima are referred to as super- and hyperdeformed [5].

Theoretical calculations of fission barriers in U and Th nuclei tend to predict shallow or nonexistent third minima, especially in the heavier isotopes such as ^{232}Th and ^{238}U. Theoretical results by McDonnell *et al.* [6] highlight the role of shell corrections in the prominence of the third minima for Th and light U isotopes. These self-consistent calculations were performed using finite-temperature superfluid nuclear density-functional theory with the Skyrme energy density functionals SkM* and UNEDF1, the latter being optimized for fission studies. A shallow third minimum was observed in the lightest Th and U isotopes, with at most a very shallow third minimum or shoulder in the ^{232}Th and ^{232}U barriers. The cause of the neutron number N dependence is identified as a neutron shell effect that reduces the third outer barrier, making the third minimum increasingly shallow with increasing N. The calculations were limited to ^{226,228,230,232}Th and ^{228,230,232,234}U, but the clear trend with increasing N leads to a prediction of no third minimum in ^{238}U. These results are at odds with the relativistic mean field (MDC-RMF) model calculations of Zhao *et al.* [7] which show shallow but well-formed 0.5- and 1.11-MeV-deep third minima in the fission barrier in ^{232}Th and ^{238}U, respectively. A shallow third minimum in ^{232}Th is also supported by the macroscopic-microscopic calculations of Jachimowicz *et al.* [5], using for the first time an eight-dimensional PES for that nucleus. After a proper inclusion of the dipole deformation, the depth of the third minimum was determined to be about 0.36 MeV. The authors conclude that a new experimental study dedicated to hyperdeformation in ^{232}Th is essential for the understanding of the third minima in actinide nuclei.

In contrast with the shallow third minima favored by theoretical models, a new paradigm of the triple-humped fission barrier with a deep hyper-deformed third minimum for U and Th isotopes was developed from experimental data. When the double-humped fission barrier was initially established [8,9] for the lighter actinide isotopes, the

---

[*] silano1@llnl.gov

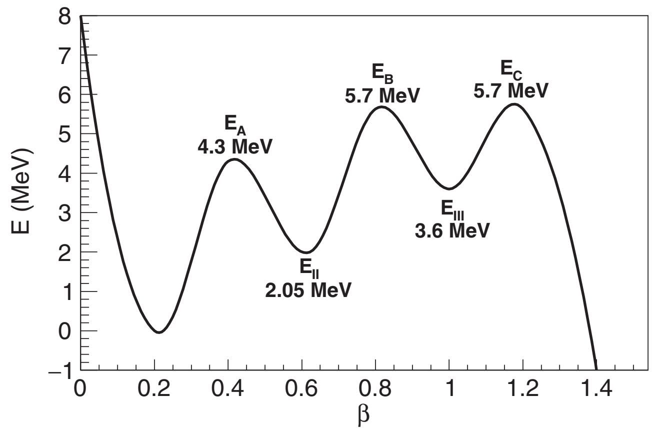

FIG. 1. A triple-humped interpretation of the ^{238}U fission barrier based on barrier parameters from Ref. [4]. The barrier parameters were determined by reproducing the experimentally measured photofission reaction cross section with statistical model calculations.

so-called "thorium anomaly" persisted. Strong transmission resonances were observed for Th nuclei, which pointed to equal heights of the inner and outer fission barrier [10]. However, the systematics of the fission barriers (and their theoretical predictions) suggested instead a much lower inner barrier than the outer one. In this context a triple-humped fission barrier was introduced assuming only a shallow third potential minimum. Almost two decades later it has been demonstrated with data from light-ion-induced fission reactions that the outer third minimum for ^{232,234,236}U is in fact as deep as the second minimum [1–3]. Most recently, photofission cross-section measurements performed by Csige *et al.* [4] on ^{238}U indicated a 2-MeV-deep third well in the ^{238}U fission barrier, as shown in Fig. 1. However, while these data were interpreted to show pronounced preference for a triple-humped barrier in ^{238}U, low statistics at near threshold energies did not allow for a precise mapping of the resonance structure of the cross sections near threshold.

The experimental support for deep third minima in Th isotopes is more conflicted. Neutron-induced fission measurements by Blons *et al.* [11–13] indicated a shallow third minimum of less than 0.5 MeV in the ^{230,231,233}Th fission barriers. However, a deep third minimum of ∼2 MeV in the ^{232}Th fission barrier was obtained by Blokhin and Soldatov [14] by analyzing photofission cross sections extracted from data obtained by unfolding bremsstrahlung beams [15]. In light of the experimental evidence of deep third minima in the fission barriers of U isotopes, older ^{232}Th photofission data [16] was reinterpreted by Thirolf *et al.* [17] to tentatively show a ∼4-MeV-deep third minimum, roughly equal in depth to the second minimum. The prospects for further re-analysis of older ^{232}Th photofission cross-section data are limited by the large discrepancies between data sets, particularly in the subbarrier energy region where the effects of the fission barrier structure are most pronounced [18].

Photofission, which is the tool used in the present work, has proven to be a valuable probe of the fission barrier structure since an incident γ-ray photon brings a single unit of angular momentum into the fissioning system. Additionally, at energies near the fission barrier, the γ-ray photon interacts with the nucleus primarily through $E1$ transitions, greatly reducing the number of fission channels that contribute to the measured data. This is especially true for even-even nuclei such as ^{232}Th and ^{238}U, which have a $J^{\pi} = 0^{+}$ ground state and thus can only be connected to a 1^{-} state by an $E1$ excitation. Recently, Mueller *et al.* [19] probed the spin and parity distribution of the fissioning compound nucleus in a number of actinides including ^{232}Th and ^{238}U by measuring polarization asymmetries in the angular distribution of prompt-photofission neutrons induced by linearly polarized γ-ray beams. However, these measurements were limited primarily to energies above the fission barrier.

Currently, there are very few photofission data at low γ-ray energies where the effects of the fission barrier are most apparent, and there are significant discrepancies in some of the existing data sets. A majority of the available data comes from measurements performed by using bremsstrahlung beams, meaning that the cross section data depend on the specific method of unfolding the beam spectrum applied to the measured fission yields. It is the aim of the present work to provide data that will help to better constrain the shape of the fission barrier through measurements of the photofission process on ^{232}Th and ^{238}U targets. Photofission was investigated with linearly polarized γ-ray beams with energies between 4.3 and 6.0 MeV, and prompt-fission neutrons were detected to measure the photofission cross sections, photofission neutron polarization asymmetries, and prompt-fission neutron multiplicities. A majority of the existing photofission data was obtained by using bremsstrahlung beams. The present measurements were made with quasimonoenergetic γ-ray beams, thus avoiding potential systematic error introduced by a beam-energy deconvolution process.

II. EXPERIMENT

A. γ-ray beams

Photofission measurements were performed at the High Intensity γ-ray Source (HIγS), at the Triangle Universities Nuclear Laboratory (TUNL). The HIγS facility [20] produces intense, quasimonoenergetic, 100% linearly polarized γ-ray beams by Compton back-scattering free-electron-laser (FEL) photons off of relativistic electrons. For this work, γ-ray beams were produced in the range of 4.3–6.3 MeV with an energy resolution of $\leqslant 3\%$ and a typical flux on target of $\sim 10^{8} \gamma/\mathrm{s}$. The accelerator was operated with 780 nm FEL photons, electron storage ring energies of 420–520 MeV and a typical electron storage ring current of 90 mA. A 12-mm-diameter, 15.24-cm-long Pb collimator was used to limit the γ-ray beam size and define the energy resolution.

The experimental setup is shown in Fig. 2. The absolute flux of the γ-ray beam was measured placing a thin sheet of plastic scintillator upstream of the main experimental target and detector assembly. The flux monitor consisted of a 10 cm × 10 cm × 1 mm sheet of polyvinyltoluene affixed to a photomultiplier tube (PMT) by a light guide. Similar

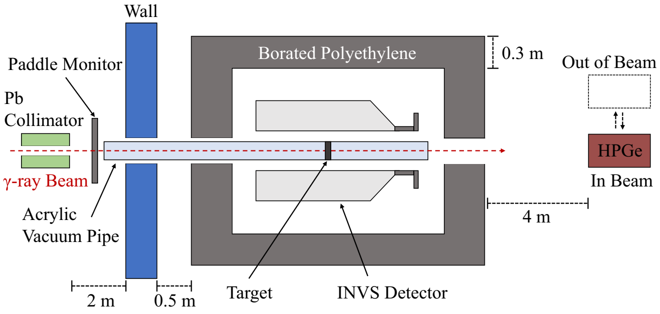

FIG. 2. Illustration of the experimental geometry. The target was mounted in a vacuum pipe inserted through the center of the INVS neutron detector. Borated polyethylene neutron shielding surrounded the detector. An upstream scintillating paddle monitored the γ-ray beam flux, while a downstream HPGe could be moved into the beam to measure the energy spectrum.

scintillating paddles were characterized as HIγS γ-ray beam flux monitors by Pywell *et al.* [21]. The energy spectrum of the incident γ-ray beam was measured with a 120% efficiency high-purity germanium detector (HPGe). The HPGe was mounted on a movable platform allowing it to be positioned off axis during the main photofission runs and in the γ-ray beam to measure the energy spectrum. In these measurements copper attenuators were placed upstream of the collimator to reduce the γ-ray beam flux and consequently the HPGe dead time to reasonable levels.

B. Targets

Table I lists the properties of the ^{232}Th, ^{238}U, ^{nat}Pb and D_2O targets used in this work. The ^{232}Th target consisted of five identical disks of 2.00 mm thickness and 25.40 mm diameter. The disks are made of ^{nat}Th which is 99.98% ^{232}Th and contains only trace amounts of $^{227-231,234}$Th. The ^{238}U target was composed of eight disks of depleted uranium with thicknesses varying from 0.55 to 0.81 mm. The ^{nat}Pb target served as a "blank" to measure γ-ray-beam-induced backgrounds, and was machined to be comparable in areal density to the ^{232}Th and ^{238}U targets. A cylindrical D_2O cell made with an acrylic casing was used for characterizing the INVS detector response to neutrons from the D(γ, n) reaction.

C. Neutron detector

Neutrons were detected with a model-IV Inventory Sample neutron detector [22] (INVS), shown in Fig. 3, consisting of 18 ^{3}He proportional counters (PCs) embedded in a cylindrical shell of polyethylene moderator. The PCs had a diameter of 2.54 cm, an active length of 39 cm, and a nominal ^{3}He gas pressure of 6 atm. The PCs were arranged in two concentric rings with radii of 7.24 cm and 10.60 cm, with each ring containing nine equally spaced PCs. The polyethylene detector body was 46.2 cm long and 30.5 cm in diameter with an 8.9-cm-diameter axial cavity for placing a neutron-generating target.

TABLE I. Targets used in the experiment.

Target	Mass (g)	Enrichment (%)	Thickness (mm)
^{232}Th	59.5 ± 0.1	99.98	10.00 ± 0.02
^{238}U	53.67 ± 0.01	>99	5.06 ± 0.03
^{nat}Pb	91.9 ± 0.1		10.6 ± 0.1
D_2O	17.4 ± 0.02	>99.9	14.6 ± 0.1

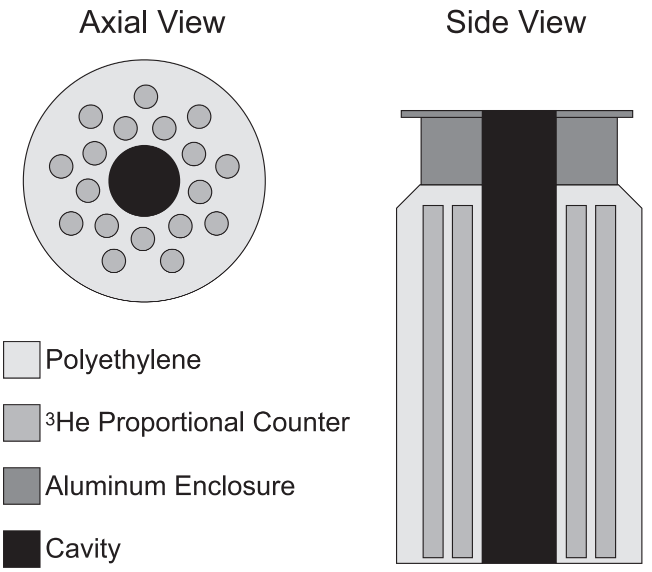

FIG. 3. Diagram of the INVS detector used in this work (not to scale).

As designed at Los Alamos National Laboratory, the INVS initially had preamplifier and discriminator circuits built into the detector. The INVS was modified for the present experiment to allow for single-tube readout by installing SHV connections with direct access to each of the PC anodes. An array of Cremat CR-110 charge-sensitive preamplifiers was mounted in a single enclosure with each preamplifier connected to a PC. The outputs of the preamplifiers were then sent to a CAEN V1730 500 MS/s 16 channel digitizer. The digitizer recorded 15 preamplifier channels, with the 16th channel reserved for a 1 Hz pulser for synchronizing digitizer time stamps and monitoring the data-acquisition (DAQ) live time.

III. DETECTOR SIMULATION AND CALIBRATION

The full experimental setup including the INVS detector, targets, target holder assembly, and detector shielding was modeled with a GEANT4 Monte Carlo simulation [23]. The simulation was calibrated with efficiency measurements of the INVS detector made by Arnold *et al.* [24]. The INVS neutron detection efficiency was measured on site by using the D(γ, n) reaction, with statistical uncertainties of 1% and systematic uncertainties of <3%. To fit the calibration data, the simulated INVS efficiency was scaled by 0.790 ± 0.003 (stat) ± 0.02 (sys) for the inner ring and 0.775 ± 0.004 (stat) ± 0.02 (sys) for the outer ring. These scaling factors account for loss of

^{3}He gas pressure over time, inefficiencies caused by the DAQ signal processing, and discriminator threshold settings.

Since the ^{3}He gas pressure, threshold settings and DAQ signal processing settings could be different for each PC, there was variation in the relative efficiency of each PC. The relative PC tube efficiencies were measured by detecting neutrons from ^{232}Th(γ, f) reaction using circularly polarized γ-ray beams, and were found to vary by $<10\%$ from the average efficiencies of the inner and outer rings.

The GEANT4 simulation was validated through measurements of neutrons from the D(γ, n) reaction using linearly polarized, 4.3 MeV γ-ray beams. This reaction generates neutrons with well-defined energy and asymmetry in the ϕ angular distribution [25,26]. The ratio of counts in the inner to outer ring of the INVS detector was measured to be 1.444 ± 0.005, in agreement with the simulated ratio of 1.46 ± 0.05. The systematic uncertainty in the simulation comes from the uncertainties in the scaling factors for the inner and outer ring efficiencies. Enough events were included in the simulation to keep the statistical uncertainties more than an order of magnitude below that of the systematics.

The angular distribution of neutrons from the D(γ, n) reaction with linearly polarized γ-ray beams has been explored in detail [25] and a simple formalism was developed to account for the polarization of the γ-ray beam [26]. A D(γ, n) reaction neutron generator was written and incorporated into the GEANT4 simulation to compare the resulting asymmetries with the measured data. The simulation and measurement data were fit with a function of the form $a(1 + b\cos 2\phi)$, where a is an overall scaling factor, b is the detected asymmetry, and ϕ is the angle of the PC relative to the polarization axis of the beam. The measurement yielded an asymmetry of 0.132 ± 0.002 for the inner ring and 0.252 ± 0.003 for the outer ring, in agreement with the simulated asymmetries of 0.132 ± 0.001 and 0.248 ± 0.002 for the inner and outer ring, respectively.

Since neutrons from a single fission event are highly correlated in angle and energy, accurately simulating the INVS detector efficiency required a source of event-by-event photofission neutrons. The Monte Carlo-based code FREYA [27] models fission observables in an event-by-event basis. By calculating neutron emission for specific instances of fission-fragment masses and excitation energies, FREYA inherently provides correlations between the various observables, including the neutron energy and angle of emission relative to the direction of the fission fragments. FREYA only supports neutron-induced and spontaneous fission of several isotopes, so it was necessary to extend the code to model photofission of ^{232}Th and ^{238}U by using the method described by Mueller *et al.* [19].

Fission product mass distributions were sampled from 0.5 MeV neutron-induced fission data [28] because suitable photofission data were not available. Fragment kinetic energies were also sampled from neutron-induced fission data, with 2.97 MeV neutrons on ^{232}Th [29] and 1.7 MeV neutrons on ^{238}U [30].

The GEANT4 simulation sampled neutrons from data sets generated by FREYA, rotating the momentum of the neutrons so that the fission-fragment axis followed the appropriate angular distribution. From the formalism described in Refs. [31,32], fission fragments induced by a linearly polarized γ-ray beam have an angular distribution of the form

$$W_f(\theta, \phi) = a_f + b_f \sin^2(\theta) + c_f \sin^2(2\theta) + P_\gamma \cos(2\phi)[b_f \sin^2(\theta) + c_f \sin^2(2\theta)], \quad (1)$$

where θ is the angle relative to the beam axis, ϕ is the azimuthal angle, and P_γ is the beam polarization. Assuming 100% linear polarization [20] and neglecting the quadrupole contribution, the expression simplifies to

$$W_f(\theta, \phi) = a_f + b_f \sin^2(\theta) + b_f \cos(2\phi) \sin^2(\theta), \quad (2)$$

where a_f and b_f are normalized such that $a_f + b_f = 1$. Equation 2 can also be used to fit the angular distribution of the neutrons emitted by the fragments to give the correlation between the fragment distribution the neutron distribution. In this paper, the angular distribution is specified as being for the fission fragments or fission neutrons by the use of the subscripts f and n, respectively.

IV. DATA REDUCTION AND ANALYSIS

A. Pulse-shape discrimination

The digitized waveforms of the preamplifier outputs of the PCs were analyzed offline. When a trigger occurred in any channel the digitizer recorded a 4.1-μs-long, 2050 sample trace for all 16 channels. In addition each trigger had an associated timestamp based on a 125 MHz internal clock in the digitizer. A 1 Hz pulser in one of the digitizer channels served as the DAQ live time monitor. The maximum trigger rate that the digitizer could handle without data loss was approximately 1 kHz, so caution was taken to keep the trigger rate below ~500 Hz by limiting the γ-ray beam flux with attenuators at higher energies where the photofission cross sections were greater. As long as the trigger rate was kept reasonable, the 1 Hz pulser consistently indicated no dead time.

^{3}He-based PCs are relatively insensitive to γ rays, but the large γ-ray beam flux of $\sim 10^8$ γ/s provided by HIγS combined with a thick actinide target created a detectable background of Compton-scattered γ rays. The scattered γ rays interact with the PCs primarily by scattering electrons into the active gas volume. These γ-ray-induced events have the potential to produce pulses with a sufficiently large amplitude that they overlap with the pulse-height spectrum from neutron-induced events, in which a proton and triton created by the ^{3}He$(n, p)^3$H reaction deposit a maximum of 763.8 keV into the active gas volume of the PC.

Identification of neutron and γ-ray detection events was achieved through the use of a pulse shape discrimination (PSD) technique originally developed for ^{3}He proportional counters in low-background experiments [33]. This technique exploits the difference in stopping power between the ions in a neutron detection event and the electron in a γ-ray detection event. For the same energy deposited, the proton and triton will have a shorter track length than the electron, and thus a shorter pulse rise time.

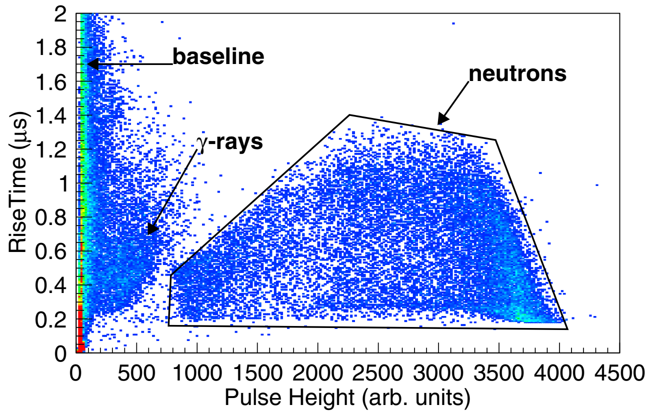

FIG. 4. PSD plot from a PC tube for a γ-ray beam incident on a ^{232}Th target, with a neutron cut region.

Following the application of a Gaussian smoothing routine to reduce high-frequency noise, the rise time, pulse height, and timestamp of each digitized waveform were extracted. The rise time was defined as the time for a pulse to rise from 10% to 50% of its maximum pulse height above the baseline. Figure 4 shows the PSD cut used for one of the ^{3}He proportional counters. The neutron and γ-ray-event regions are well separated in rise time vs pulse-height space. Measurements made with a $^{\mathrm{nat}}$Pb target for generating Compton-scattered γ rays and a deuterium target for generating neutrons confirmed the particle identification regions in the PSD plot. Events in the baseline noise region occur because the analysis code attempts to extract pulse characteristics from each digitizer channel, regardless of which channel triggered the DAQ since coincident neutron detections happened regularly. In the absence of a neutron or γ-ray event waveform, the analysis routine extracts pulse characteristics from random noise.

B. Background neutron multiplicity analysis

Determining the detected neutron multiplicities requires setting a time window in which neutrons from the same fission event may be counted. The time window must be long enough that any correlated neutrons from a single fission event will have either been detected or escaped the detector; however, making it excessively long increases the likelihood that uncorrelated neutrons from other fission events or backgrounds are counted as well. Thus a clear understanding of the neutron detection timescale is necessary.

GEANT4 simulations of the INVS detector were performed and the detection time for each neutron was recorded, where the neutron is always emitted at time $t = 0$ and detected some time after that. The simulated neutron detection time distribution was found to be well represented by an exponential decay function with a 31 μs half-life fit. A direct comparison of neutron detection time cannot be generated from the experimental data because there is no "start" signal for each fission event. The closest comparison is to instead sort through the detected neutrons in chronological order, with the first detected neutron creating a gate and subsequent neutron detection times recorded relative to the first one. A 1-ms-long gate was used to guarantee that all detected neutrons from the fission event were included. The analysis was applied to Monte Carlo simulation data and experimental data from the ^{238}U(γ, f) reaction at $E_\gamma = 5.1$ MeV, an energy at which the photofission rate was much larger than the background event rate but still sufficiently low that coincident fission events were rare. Figure 5 shows the good agreement between the time distributions for simulated and detected photofission neutrons in the INVS detector, validating the neutron detection time response of the GEANT4 simulation.

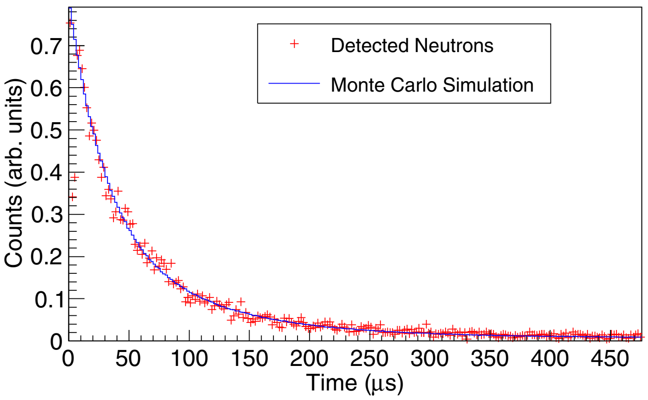

FIG. 5. Comparison of experimental data and a Monte Carlo simulation of neutron time distributions in the INVS detector for the ^{238}U(γ, f) reaction at $E_\gamma = 5.1$ MeV.

There were three sources of background neutrons present throughout this work: cosmic-ray-induced neutrons, neutrons from the D(γ, n) reaction occurring in the detector moderator, and neutrons from bremsstrahlung contamination in the HIγS beam [34] inducing (γ, xn) and (γ, f) reactions on the targets. Sources of background neutrons were differentiated with a multiplicity analysis technique. Background multiplicities were defined by grouping together neutrons within 300 μs coincidence windows, where the first detected neutron defines the start of the coincidence gate. The multiplicity was defined as the total number of neutrons in the gate, including the one which triggered it, meaning that the minimum detected multiplicity was 1 by definition. The next 300 μs long gate was created on the first neutron that fell outside of the previous gate so that any neutron was only counted towards one multiplicity event. The observed neutron multiplicity distributions for the various backgrounds are shown in Fig. 6.

The cosmic-ray-induced neutron background was reduced to a neutron detection rate of 0.537 ± 0.003 Hz by surrounding the INVS detector with ~30 cm of borated polyethylene shielding on all sides.

A bremsstrahlung component of the γ-ray beam was identified by placing a $^{\mathrm{nat}}$Pb target in the INVS detector and operating HIγS in "single-bunch mode," in which a single electron bunch was held in the FEL storage ring instead of the two used in normal operation [20]. In this configuration there are no counterpropagating electrons so the HIγS facility is incapable of generating γ rays by Compton scattering the FEL photons. Furthermore, the configuration of the HIγS facility was such that γ rays generated by Compton-scattered FEL photons would have been below the threshold for $^{\mathrm{nat}}$Pb(γ, xn) reactions. Determining the properties of the bremsstrahlung beam

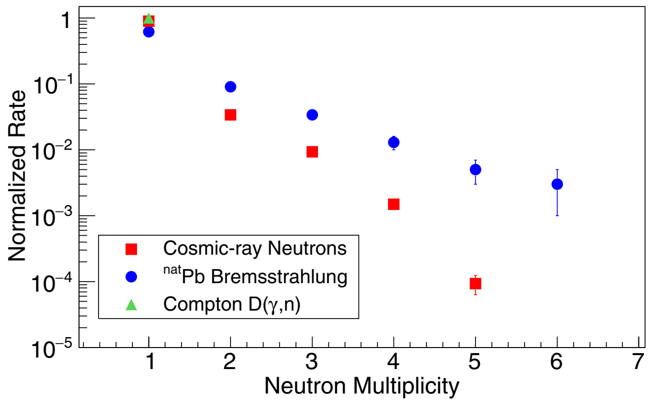

FIG. 6. Neutron multiplicity rates, normalized to 1 Hz, from backgrounds caused by cosmic-ray-induced neutrons, bremsstrahlung contamination of the γ-ray beam inducing $^{\text{nat}}\text{Pb}(\gamma, xn)$ reaction neutrons, and Compton-scattered γ rays inducing $\text{D}(\gamma, n)$ reaction neutrons in the polyethylene moderator of the INVS detector.

is beyond the scope of this work. We sought to only measure the directly observable effects of the bremsstrahlung: the neutron detection rates and detected neutron multiplicity distribution. The observed bremsstrahlung-induced $^{\text{nat}}\text{Pb}(\gamma, xn)$ neutron multiplicity distribution is shown in Fig. 6, with a typical neutron detection rate of ~0.75 to 1.5 Hz.

The combined bremsstrahlung and Compton-scattering-induced backgrounds were measured by placing a $^{\text{nat}}\text{Pb}$ target in the INVS detector and running HIγS in the standard “two-bunch mode” which produces an intense, quasimonoenergetic γ-ray beam. The observed neutron multiplicity distributions were fit with neutrons from the $^{\text{nat}}\text{Pb}(\gamma, xn)$ reaction and Compton scattering $\text{D}(\gamma, n)$ reaction multiplicity distributions to determine the contributions from the two backgrounds, with typical uncertainties of $\leqslant 10\%$. The background neutron detection rates as a function of E_γ are shown relative to the primary γ-ray-beam flux in Fig. 7. The Compton scattering $\text{D}(\gamma, n)$ reaction and bremsstrahlung (γ, xn) reaction backgrounds were both scaled appropriately for the ^{232}Th and ^{238}U targets. The Compton-scattering component scales with the number of electrons in the target nuclei, the target thickness and density. The bremsstrahlung component was multiplied by scaling factors for each target which were experimentally measured using the single-bunch mode HIγS operation.

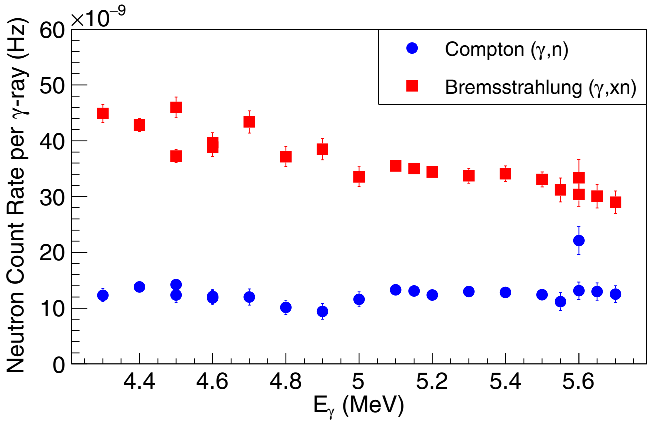

FIG. 7. HIγS beam-induced background neutron count rates observed with a $^{\text{nat}}\text{Pb}$ target, normalized to the flux of the primary γ-ray beam.

C. Prompt-fission neutron multiplicity analysis

Defining the detected neutron multiplicities by grouping together neutrons within a 300 μs window works well for the low event rates in the background analysis (see Sec. IV B) but suffers from pileup effects for the higher event rates of photofission measurements. Consequently, the prompt-fission neutron analysis relied on the Rossi-alpha method [35], a multiplicity logic scheme originally developed for reactor neutron noise analysis. This method is more robust against accidental coincidences caused by high fission rates.

The gating logic used in the present work was as follows: after a neutron detection, there was a 10 μs delay to account for a small dead time immediately following the digitizer gate. Next, a 500-μs-long gate was set which contained real and accidental coincidences (RA), and following that a 500-μs-long gate which should only contain accidental coincidences (A). Each neutron detection created the RA and A gates, and the number of events of each multiplicity was given by RA-A, the difference between the real events plus accidental events and just the accidentals.

Even with the Rossi-alpha multiplicity gating logic, the detected neutron multiplicity distributions depend on the fission event rate and overlap with the background in a nonlinear manner. A Monte Carlo simulation was developed to fit the prompt-fission neutron multiplicity distribution with the detected Rossi-alpha multiplicities. The fission neutron multiplicity distribution was modeled as a Gaussian distribution [36] with the fit-parameters mean $\overline{\nu}$ and spread σ. The Monte Carlo simulation modeled the detection of the photofission neutrons with the assumed initial distribution, added the background events with the experimentally measured multiplicities and rates (see Sec. IV B), and analyzed the resulting data stream using the Rossi-alpha gating logic. The multiplicity distribution parameters $\overline{\nu}$ and σ were varied to minimize the χ^2 between the measured and the Monte Carlo simulated RA-A distributions.

D. Neutron asymmetry analysis

After subtracting background counts and correcting for the relative PC efficiencies, the detected prompt-photofission neutron asymmetries were measured by fitting the relative yields of each PC tube with the function

$$Y_d(\phi) = a_d[1 + b_d \cos(2\phi)], \tag{3}$$

where $Y_d(\phi)$ is the detected neutron yield in the PC tube at angle ϕ, a_d is an overall scaling factor, and b_d is the detector asymmetry. Figure 8 shows examples of the fit, performed independently on the inner and outer rings of the INVS detector.

The simulated correlation between the detected neutron asymmetry b_d and the emitted neutron asymmetry b_n is shown in Fig. 9, where b_n is defined in Eq. (2). GEANT4 simulations were performed by using the photofission neutrons from the FREYA calculations for both ^{238}U and ^{232}Th, with each unique target geometry modeled to account for neutron scattering in the target and target holder assemblies. Since the inner and outer rings of the INVS detector have different detected asymmetry responses to the same emitted neutron angular distribution, data from each ring was treated as a separate measurement of the polarization asymmetry and the results were combined for a single measurement for each E_γ and target. There was no strong dependence observed between the fissioning isotope species and the detector response to the neutron asymmetry, which is consistent with the results of Ref. [19].

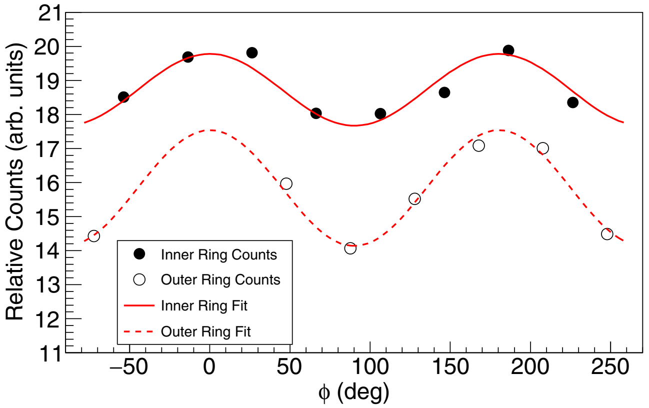

FIG. 8. Detected neutron yields and asymmetry in the inner and outer rings of PC tubes in the INVS detector for $E_\gamma = 5.6$ MeV on a ^{238}U target. The outer ring counts have been multiplied by a factor of 1.3 to appear on the same scale as the inner ring. Statistical error bars are smaller than the markers.

E. Photofission-cross-section analysis

The photofission cross section is written as

$$\sigma(\gamma, f) = \frac{(N_n - N_b)A_t}{\epsilon_{\rm INVS}\bar{\nu}N_\gamma \ell_t \rho_t f N_A}, \tag{4}$$

where N_n is the total number of detected neutrons, N_b is the number of background neutrons, A_t is the atomic mass of the target nuclei, $\epsilon_{\rm INVS}$ is the efficiency of the INVS detector, $\bar{\nu}$ is the mean prompt-neutron multiplicity, N_γ is the total number of γ rays on target, ℓ_t is the target thickness, ρ_t is the target density, f is a factor which accounts for the attenuation of the γ-ray beam within the thick target, and N_A is Avogadro's number. The thick-target-correction factor is written as

$$f = \frac{1 - e^{-\mu\rho_t\ell_t}}{\mu\rho_t\ell_t}, \tag{5}$$

where μ is the attenuation coefficient of the target material [37]. N_b is determined by using the multiplicity analysis technique described in Sec. IV C.

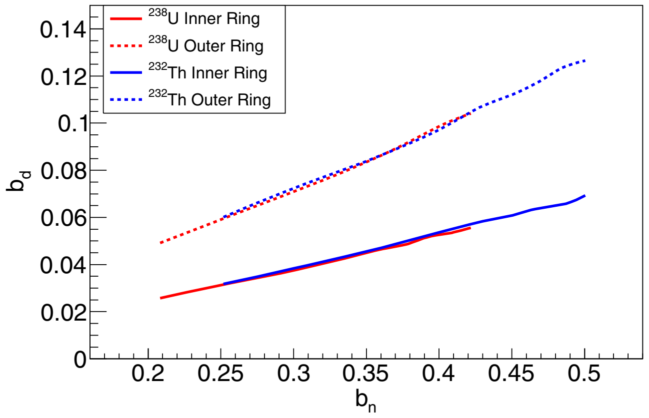

FIG. 9. Simulated correlation between the detected asymmetry b_d and emitted neutron polarization asymmetry b_n for the ^{238}U and ^{232}Th photofission neutrons.

The photofission neutron spectra from the FREYA calculations did not differ enough over the range of 4.3 MeV $< E_\gamma <$ 6.0 MeV to change the simulated efficiency of the INVS detector. Thus, $\epsilon_{\rm INVS} = 0.295 \pm 0.009$ for the ^{232}Th(γ, f) neutrons and $\epsilon_{\rm INVS} = 0.277 \pm 0.008$ for the ^{238}U(γ, f) neutrons. The values of $\bar{\nu}$ for ^{232}Th(γ, f) and ^{238}U(γ, f) were determined by taking the weighted average of the multiplicity measurements results for each target (see Sec. V B). The photofission–cross-section analysis in this work uses $\bar{\nu}_{\rm mean} = 2.22\pm^{0.02}_{0.05}$ and $\bar{\nu}_{\rm mean} = 2.46\pm^{0.01}_{0.03}$ for ^{232}Th and ^{238}U, respectively. The ~3% systematic error in the photofission-cross-section data includes contributions from $\epsilon_{\rm INVS}$ (3%), target thickness (0.2% for ^{232}Th, 0.6% for ^{238}U, 1% for $^{\rm nat}$Pb, and 0.7% for D$_2$O) and mean neutron multiplicities (0.4%–2%).

V. RESULTS AND DISCUSSION

A. Prompt-photofission neutron polarization asymmetries

The measured prompt-photofission polarization asymmetries are shown in Fig. 10 for ^{238}U and ^{232}Th, and are qualitatively consistent with the expected effects of the transmission through the fission barrier. Based on the most likely energy level ordering for an even-even nucleus [38], the lowest energy $J^\pi = 1^-$ excitation is $(J^\pi, K) = (1^-, 0)$, which corresponds to the mass asymmetry mode. This would then be the dominant fission channel at low E_γ and would result in large polarization asymmetries. The next lowest channel would be the $(1^-, \pm 1)$ bending mode which would begin to contribute as E_γ is increased, reducing the polarization asymmetry, as experimentally observed.

In Fig. 11 the present asymmetry results are compared with the data of Mueller *et al.* [19], the only other measurement of photofission neutron polarization asymmetries in ^{238}U and ^{232}Th. Since liquid scintillator neutron detectors were used in Ref. [19], the presented data were limited to neutrons above $E_n = 1.5$ MeV. To make a direct comparison with the prior data, the present asymmetry calculations were adjusted to include only neutrons above $E_n = 1.5$ MeV. This adjustment was achieved by setting a 1.5 MeV energy threshold on the neutron distribution fit which correlates the fission-fragment asymmetry with the emitted neutron asymmetry. Omitting the lower-energy neutrons increases b_n by about 10% since the neutrons which are emitted in the direction of the fragment receive more of a kinematic boost and therefore tend to

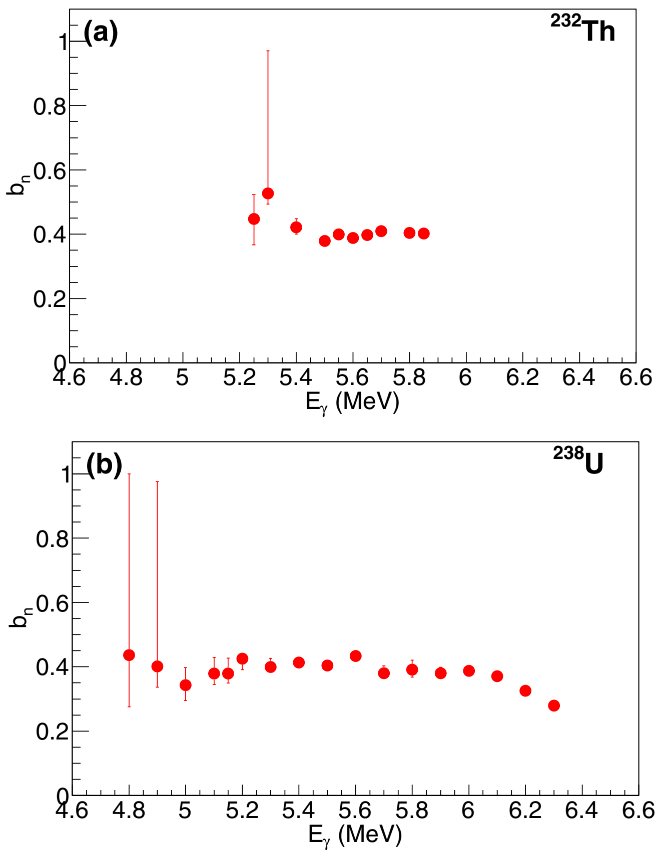

FIG. 10. Photofission neutron polarization asymmetries for (a) ^{232}Th and (b) ^{238}U. The error bars reflect the fit error from Eq. (3).

have higher energies than those emitted perpendicular to the fragment motion. Once the effects of the neutron energy cut of $E_n > 1.5$ MeV are accounted for, there is excellent agreement between the present results and the data of Mueller *et al.* in the energy region where they overlap.

B. Prompt-photofission neutron multiplicities

The mean prompt-photofission neutron multiplicities, $\overline{\nu}$, for ^{232}Th and ^{238}U are shown in Fig. 12, along with previous measurements [39,40], the ENDF/B-VII.1 evaluation [41], and an empirical model developed by Lengyel *et al.* [42]. The error bars in the present data represent the range of values that increase the χ^2 of the fit by less than 1. A weighted mean of the present data was calculated by using the inverse of the χ^2 as the weighting factor. Multiplicities determined in the present work are $\overline{\nu}_{\mathrm{mean}} = 2.22\pm^{0.02}_{0.05}$ and $\overline{\nu}_{\mathrm{mean}} = 2.46\pm^{0.01}_{0.03}$ for the photofission of ^{232}Th and ^{238}U, respectively. The lowest E_γ points which diverge from the rest of the data suffer from poor statistics and consequently have larger χ^2 values exceeding 200 and 50 for the lowest E_γ measurements for ^{232}Th and ^{238}U, respectively. In the case of ^{232}Th, the present data are in better agreement with Findlay *et al.* [40] than with the data of Caldwell *et al.* [39]. The measurements of Ref. [39] appear systematically low in comparison, along with the ENDF/B-VII.1 evaluation [41] and the empirical model [42].

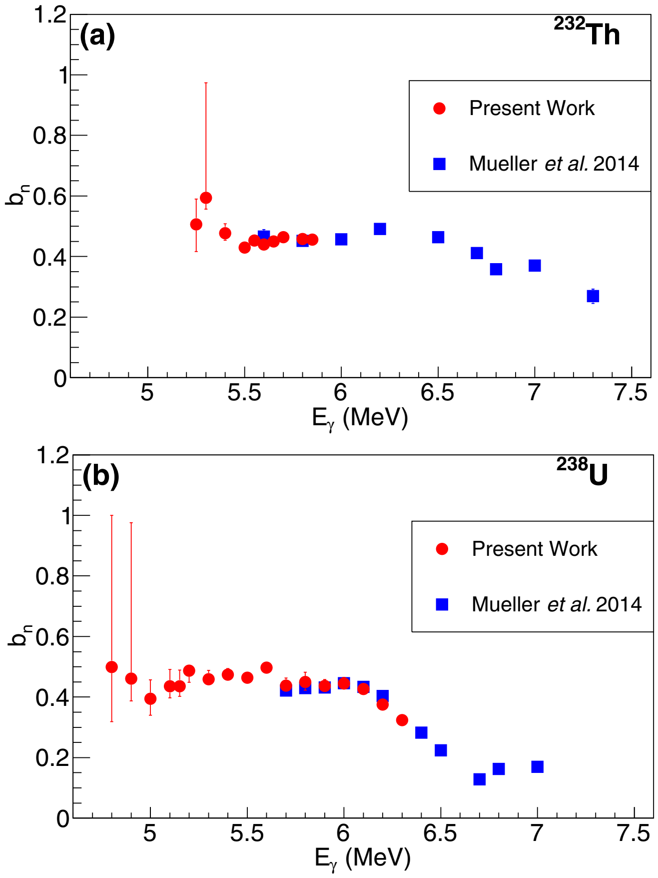

FIG. 11. Photofission neutron polarization asymmetries in (a) ^{232}Th and (b) ^{238}U for neutrons with $E_n > 1.5$ MeV, compared with the data of Mueller *et al.* [19].

In the case of ^{238}U, the present data are in good agreement with the data of Ref. [39], the ENDF/B-VII.1 evaluation [41], and the empirical model of Ref. [42].

The spreads of the Gaussian prompt-neutron multiplicity distributions σ are plotted in Fig. 13, in good agreement with the only previous measurement in a comparable E_γ range [39]. The χ^2 weighted means were measured to be $\sigma_{\mathrm{mean}} = 1.25\pm^{0.02}_{0.01}$ and $\sigma_{\mathrm{mean}} = 1.36\pm^{0.02}_{0.01}$ for ^{232}Th and ^{238}U, respectively.

C. Photofission cross sections

The ^{232}Th(γ, f) reaction-cross-section results are listed in Table II and plotted in Fig. 14, along with all available literature data sets which extend below an excitation energy of 6 MeV [15,16,40,43–46] and the ENDF/B-VIII.0 evaluation [47]. Data sets consistent with 0 mb below ~6 MeV [48–52] were omitted.

There is some tension between the present data and the ENDF/B-VIII.0 evaluation, with the present data about an order of magnitude higher in the 5.2–5.5 MeV range. In this region, the cross section in the ENDF/B-VIII.0 evaluation is lower than nearly all of the available experimental data. The present results are generally in good agreement with the data obtained by using bremsstrahlung beams [15,40,43–45]. In particular, the present work observes the same plateau in the

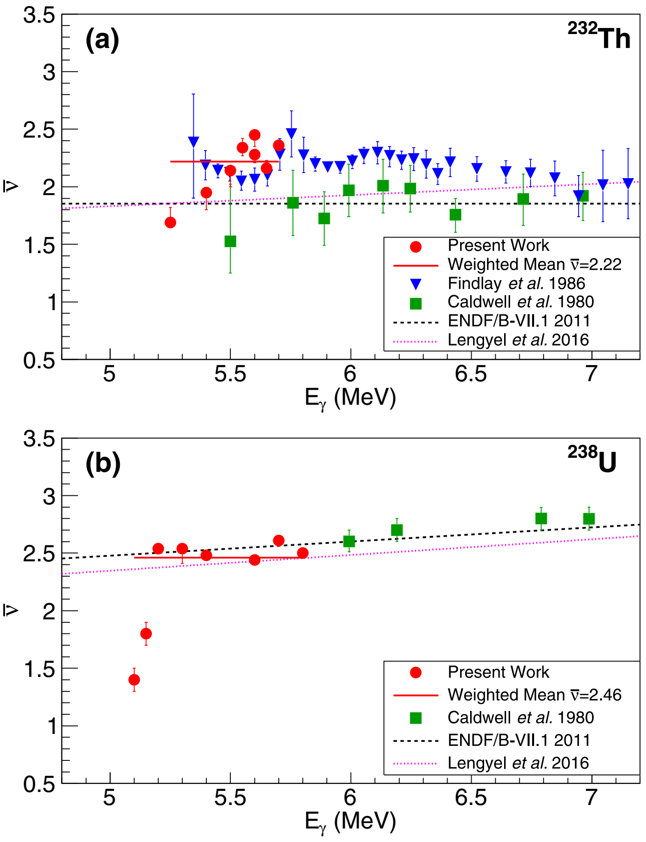

FIG. 12. Measured mean photofission neutron multiplicities for (a) ^{232}Th and (b) ^{238}U compared with the data of Caldwell *et al.* [39], Findlay *et al.* [40], the ENDF/B-VII.1 evaluation [41], and the empirical model of Lengyel *et al.* [42].

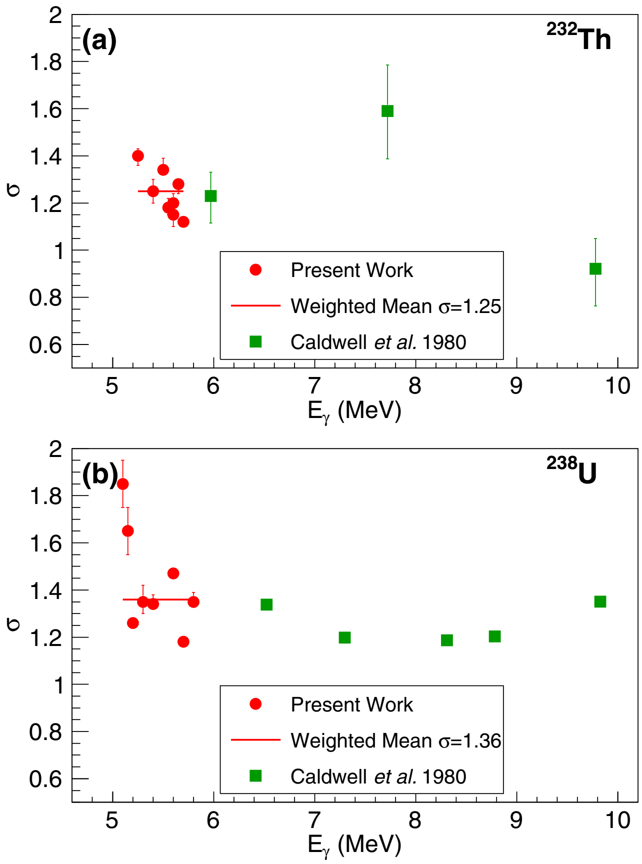

FIG. 13. Measured spreads of the prompt-neutron multiplicity distributions for (a) ^{232}Th and (b) ^{238}U, compared with the data of Caldwell *et al.* [39].

photofission cross section of ^{232}Th in the E_γ range of 5.4 to 5.7 MeV. Blokhin and Soldatov [14] attribute this plateau to an almost-complete fragmentation of a resonance in the second minimum caused by damping, and a partial fragmentation of a resonance in the third minimum which is shifted in energy relative to the second minimum resonance. This combination of resonant states in the second and third minima explains the large width of the plateau and the presence of resonance structure. However, the 5.6 MeV resonance observed in the data of Smirenkin and Soldatov [15] is not seen in the present results. This resonance is also not apparent in the only other data measured with quasimonoenergetic γ-ray beams in that energy region [46]. Despite the absence of the 5.6 MeV resonance in the present results, the 5.4 to 5.7 MeV plateau that is apparent in all available data sets is difficult to explain without damped vibrational states, which is suggestive of a deep third minimum in the fission barrier.

TABLE II. Tabulated ^{232}Th(γ, f) reaction-cross-section data. The measurements were performed with Gaussian γ-ray beam spectra with mean E_γ and spread σ_{E_γ}. The quoted errors are the statistical uncertainties, and there is an additional overall 3% systematic error.

E_γ (MeV)	σ_{E_γ} (MeV)	$\sigma(\gamma, f)$ (μb)
4.7	0.071	−0.4 ± 0.2
4.8	0.072	−0.04 ± 0.1
4.9	0.074	−0.4 ± 0.1
5.0	0.075	0.30 ± 0.07
5.1	0.077	0.27 ± 0.06
5.2	0.078	3.73 ± 0.09
5.25	0.079	7.4 ± 0.2
5.3	0.080	22.7 ± 0.2
5.4	0.081	92.9 ± 0.3
5.5	0.083	203.8 ± 0.5
5.55	0.083	227.3 ± 0.5
5.6	0.084	248.0 ± 0.5
5.65	0.085	235.1 ± 0.5
5.7	0.089	277.1 ± 0.5
5.8	0.087	799 ± 3

The ^{238}U(γ, f) reaction-cross-section results are listed in Table III and plotted in Fig. 15, along with all available literature data sets which extend below an excitation energy of 6 MeV [4,43,45,46,49,51–57] and the ENDF/B-VIII.0 evaluation [47].

The present results are in good agreement with the data of Ostapenko *et al.* [55], Zhuchko *et al.* [45], and Soldatov and Smirenkin [56] obtained by using bremsstrahlung beams. Additionally, the present results are in remarkably good agreement with the ENDF/B-VIII.0 evaluation.

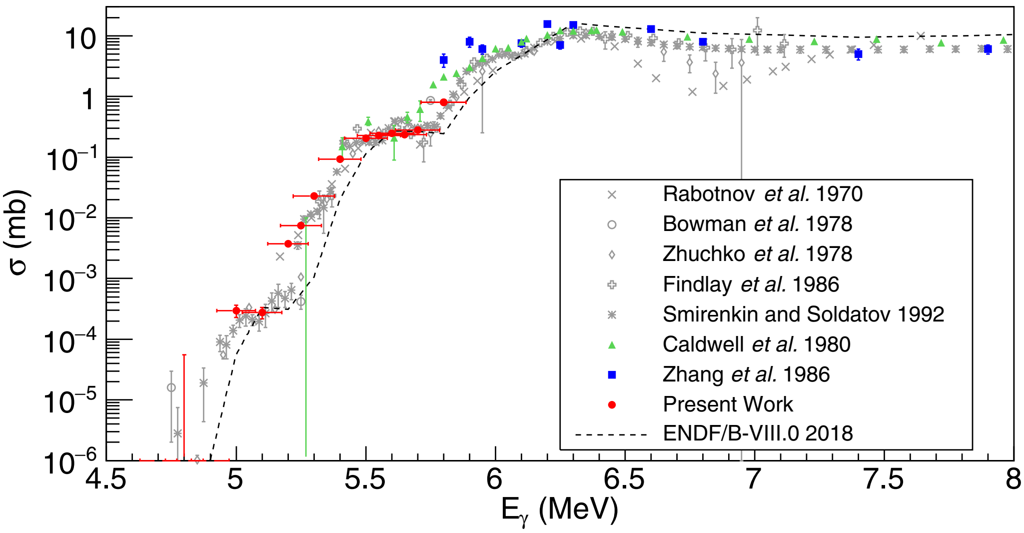

FIG. 14. The measured photofission cross section of ^{232}Th (red circles) compared with data obtained by using bremsstrahlung γ-ray beams (various gray markers) [15,40,43–45], data obtained by using quasimonoenergetic γ-ray beams (green triangles, blue squares) [16,46], and the ENDF/B-VIII.0 evaluation (dashed line) [47]. Vertical error bars represent statistical uncertainty and horizontal bars represent the energy resolution of the γ-ray beams.

The present ^{238}U(γ, f) reaction-cross-section data are consistent with the data of Csige *et al.* [4] above $E_\gamma \approx$ 5.3 MeV; however, there is increasing disagreement between the data sets below this energy, with a factor of ~3 discrepancy at 4.8 MeV. Because the data of Ref. [4] were also obtained at the HIγS facility by using nominally the same γ-ray beams as in the present work, there is a unique opportunity to determine the source of the inconsistency between the prior measurement and the present results. We attribute this low-energy divergence to a bremsstrahlung beam contamination present at the HIγS facility, which was previously discussed in Ref. [34]. The effects of the bremsstrahlung beam were measured precisely for the first time in this work and were not taken into account in the results of Ref. [4]. The ^{238}U photofission cross section was measured in Ref. [4] by using an array of parallel plate avalanche counters, detecting both fragments from a fission event in coincidence. Since it is not possible to distinguish fission fragments from fission induced by the two different beam components, the background from the bremsstrahlung contamination of the HIγS beam cannot be removed from the measured fission yields.

In Fig. 16 the present results are shown with and without proper subtraction of the bremsstrahlung-induced background, with the non-background-subtracted data in much

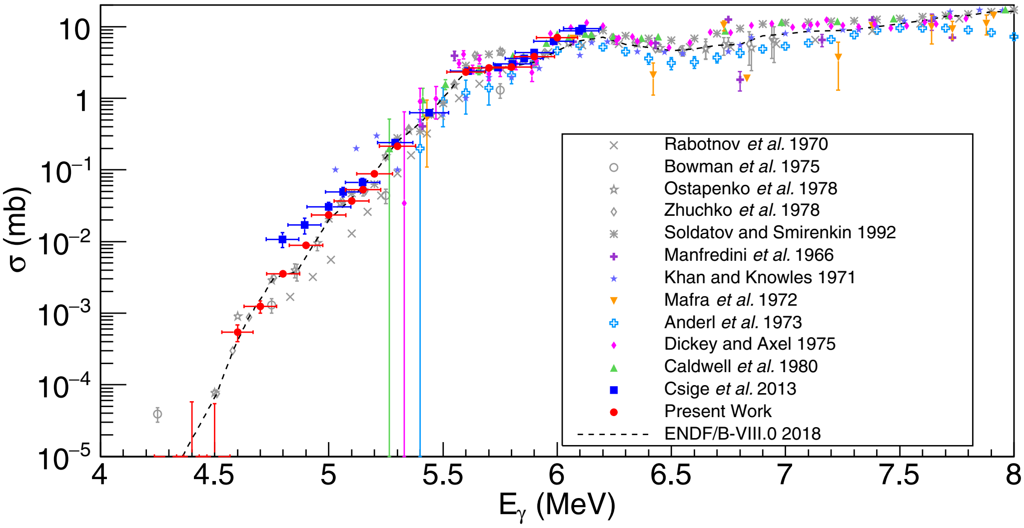

FIG. 15. Measured photofission cross section of ^{238}U (red circles) compared with data obtained by using bremsstrahlung γ-ray beams (various gray markers) [43,45,54–56], data obtained by using quasimonoenergetic γ-ray beams (purple crosses, blue stars, orange triangles, blue crosses, pink diamonds, green triangles, blue squares) [4,46,49,51–53,57], and the ENDF/B-VIII.0 evaluation (dashed line) [47]. Vertical error bars represent statistical uncertainty and horizontal bars represent the energy resolution of the γ-ray beams.

TABLE III. Tabulated ^{238}U(γ, f) reaction-cross-section data. The measurements were performed with Gaussian γ-ray beam spectra with mean E_γ and spread σ_{E_γ}. The quoted errors are the statistical uncertainties, and there is an additional overall 3% systematic error.

E_γ(MeV)	σ_{E_γ} (MeV)	$\sigma(\gamma, f)$ (μb)
4.3	0.065	−0.3 ± 0.2
4.4	0.066	−0.08 ± 0.1
4.5	0.068	−0.06 ± 0.1
4.6	0.069	0.5 ± 0.1
4.7	0.071	1.2 ± 0.2
4.8	0.072	3.5 ± 0.2
4.9	0.074	8.9 ± 0.3
5.0	0.075	23.3 ± 0.2
5.1	0.077	37.0 ± 0.2
5.15	0.077	52.7 ± 0.2
5.2	0.078	88.0 ± 0.3
5.3	0.080	215.6 ± 0.6
5.6	0.084	2330 ± 5
5.7	0.086	2639 ± 6
5.8	0.087	2722 ± 6
5.9	0.089	3798 ± 7
6.0	0.090	7060 ± 10

better agreement with the data of Ref. [4]. This agreement supports our assertion that the previously measured excess cross section at low energies was caused by the bremsstrahlung contamination of the HIγS γ-ray beam. Figure 16 also includes photofission cross sections calculated by assuming double- and triple-humped ^{238}U fission barriers by Csige *et al.* The calculations were performed with the EMPIRE 3.1 code [58], tuning the input parameters to best reproduce the measured photofission-cross-section data. Neither calculation is in good agreement with the present results; in particular the predicted resonance at 4.6 MeV, which is present in both calculations, is not observed in the present data. The discrepancy between the current ^{238}U photofission data and the calculated cross sections from Ref. [4] assuming a double- and triple- humped fission barrier casts significant doubt on the triple-humped shape of the ^{238}U fission barrier proposed in Ref. [4] and shown in Fig. 1.

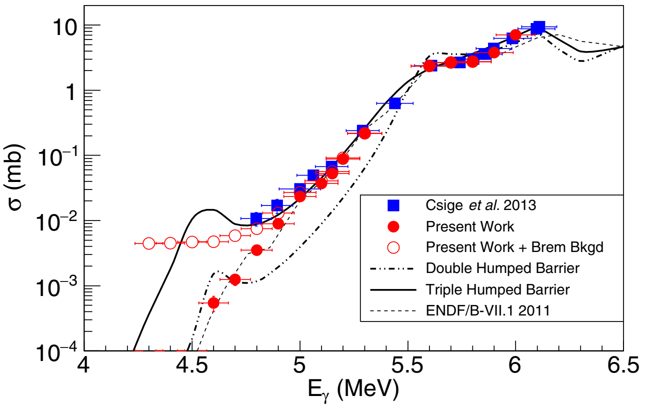

FIG. 16. ^{238}U photofission-cross-section results with and without the HIγS γ-ray beam bremsstrahlung background subtracted, compared with the data of Csige *et al.* [4] and the ENDF/B-VIII.0 evaluation [47]. Photofission-cross-section calculations from Csige *et al.* for double- and triple-humped fission barrier fits to their data are also shown.

A more definitive statement about the structure of the ^{238}U fission barrier will require new photofission-cross-section calculations tuned to fit not only the present data, but the broadest range of available data near the fission barrier. Given the good agreement between the present data obtained by using quasimonoenergetic γ-ray beams and the data of Zhuchko *et al.* [45] obtained by using bremsstrahlung beams, it is reasonable to conclude that the unfolding procedure applied to that data gives accurate results. Since the data of Ref. [45] extends down to $E_\gamma = 3.42$ MeV, these data could supplement the present data set below $E_\gamma = 4.6$ MeV, the lowest energy nonzero data point.

VI. CONCLUSIONS

High-precision measurements of the photofission cross sections, prompt-fission neutron polarization asymmetries, and the mean and spread of the prompt-fission neutron multiplicity distributions of ^{232}Th and ^{238}U have been performed in the γ-ray energy region of $E_\gamma = 4.7$ to 5.8 MeV and $E_\gamma = 4.3$ to 6.0 MeV, respectively. This work, performed by using the monochromatic, high-intensity, Compton-backscattered γ-ray beams of the HIγS facility, represents the lowest-energy measurements of this kind using quasimonoenergetic-γ-ray beams. Our results show that a previously observed shelf in the ^{238}U photofission cross section, which had been identified as a resonance caused by a deep third minimum in the ^{238}U fission barrier, is instead an accelerator background induced by a bremsstrahlung contamination of the γ-ray beam. Future measurements of the photofission cross sections of both ^{238}U and ^{232}Th would help to place additional constraints on the structure of the fission barriers of the respective nuclei, especially with regards to the debate over the existence of deep third minima. Next-generation Compton-backscatter γ-ray sources such as the ELI-NP facility [17] and the proposed HIγS2 upgrade [59] will provide γ-ray beams with the improved flux and resolution needed to measure photofission cross sections and resonances well below the fission barrier.

ACKNOWLEDGMENTS

The authors thank G. Rich for invaluable contributions to the development of this project. Additionally, we express gratitude to A. Banu and N. Parikh for their help in the experiment and data taking, and to J. Langenbrunner for providing material support. We thank the HIγS staff for delivering high-quality γ-ray beams for this work. We especially wish to thank S. Mikhailov for enlightening discussions of the γ-ray-beam properties. This work was performed under the auspices of US DOE by LLNL under contract DE-AC52-07NA27344, with support from the US DOE Office of Science, Office of Nuclear Physics through Grants No. DE-FG02-97ER41033 and No. DE-FG02-97ER41041.

[1] L. Csige, M. Csatlós, T. Faestermann, Z. Gácsi, J. Gulyás, D. Habs, R. Hertenberger, A. Krasznahorkay, R. Lutter, H. J. Maier, P. G. Thirolf, and H.-F. Wirth, Phys. Rev. C **80**, 011301(R) (2009).

[2] A. Krasznahorkay, D. Habs, M. Hunyadi, D. Gassmann, M. Csatlós, Y. Eisermann, T. Faestermann, G. Graw, J. Gulyás, R. Hertenberger, H. Maier, Z. Máté, A. Metz, J. Ott, P. Thirolf, and S. van der Werf, Phys. Lett. B **461**, 15 (1999).

[3] M. Csatlós, A. Krasznahorkay, P. Thirolf, D. Habs, Y. Eisermann, T. Faestermann, G. Graw, J. Gulyás, M. Harakeh, R. Hertenberger, M. Hunyadi, H. Maier, Z. Máté, O. Schaile, and H.-F. Wirth, Phys. Lett. B **615**, 175 (2005).

[4] L. Csige, D. M. Filipescu, T. Glodariu, J. Gulyás, M. M. Günther, D. Habs, H. J. Karwowski, A. Krasznahorkay, G. C. Rich, M. Sin, L. Stroe, O. Tesileanu, and P. G. Thirolf, Phys. Rev. C **87**, 044321 (2013).

[5] P. Jachimowicz, M. Kowal, and J. Skalski, Phys. Rev. C **87**, 044308 (2013).

[6] J. D. McDonnell, W. Nazarewicz, and J. A. Sheikh, Phys. Rev. C **87**, 054327 (2013).

[7] J. Zhao, B.-N. Lu, D. Vretenar, E.-G. Zhao, and S.-G. Zhou, Phys. Rev. C **91**, 014321 (2015).

[8] R. Vandenbosch and J. Huizenga, *Nuclear Fission* (Academic Press, New York, 1973).

[9] S. Bjørnholm and J. E. Lynn, Rev. Mod. Phys. **52**, 725 (1980).

[10] B. B. Back, H. C. Britt, J. D. Garrett, and O. Hansen, Phys. Rev. Lett. **28**, 1707 (1972).

[11] J. Blons, C. Mazur, D. Paya, M. Ribrag, and H. Weigmann, Nucl. Phys. A **414**, 1 (1984).

[12] J. Blons, B. Fabbro, C. Mazur, D. Paya, M. Ribrag, and Y. Patin, Nucl. Phys. A **477**, 231 (1988).

[13] J. Blons, Nucl. Phys. A **502**, 121 (1989).

[14] A. I. Blokhin and A. S. Soldatov, Phys. At. Nucl. **72**, 917 (2009).

[15] G. N. Smirenkin and A. S. Soldatov, Sov. J. Nuclear Phys. **59**, 185 (1996).

[16] H. X. Zhang, T. R. Yeh, and H. Lancman, Phys. Rev. C **34**, 1397 (1986).

[17] P. Thirolf, L. Csige, D. Habs, M. Günther, M. Jentschel, A. Krasznahorkay, D. Filipescu, T. Glodariu, L. Stroe, O. Tesileanu, H. Karwowski, and G. Rich, EPJ Web Conf. **38**, 08001 (2012).

[18] L. J. Lindgren and A. Sandell, Z. Phys. A: At. Nucl. (1975) **285**, 415 (1978).

[19] J. M. Mueller, M. W. Ahmed, R. H. France, M. S. Johnson, H. J. Karwowski, L. S. Myers, J. Randrup, M. H. Sikora, M. C. Spraker, S. Stave, J. R. Tompkins, R. Vogt, H. R. Weller, C. S. Whisnant, and W. R. Zimmerman, Phys. Rev. C **89**, 034615 (2014).

[20] H. R. Weller, M. W. Ahmed, H. Gao, W. Tornow, Y. K. Wu, M. Gai, and R. Miskimen, Prog. Part. Nucl. Phys. **62**, 257 (2009).

[21] R. Pywell, O. Mavrichi, W. Wurtz, and R. Wilson, Nucl. Instrum. Methods Phys. Res., Sect. A **606**, 517 (2009).

[22] J. K. Sprinkle, Jr., H. O. Menlove, M. C. Miller, and P. A. Russo, *An Evaluation of the INVS Model IV Neutron Counter*, Tech. Rep. LA-12496-MS (Los Alamos National Laboratory, Los Alamos, 1993).

[23] S. Agostinelli *et al.*, Nucl. Instrum. Methods Phys. Res., Sect. A **506**, 250 (2003).

[24] C. Arnold, T. Clegg, H. Karwowski, G. Rich, J. Tompkins, and C. Howell, Nucl. Instrum. Methods Phys. Res., Sect. A **647**, 55 (2011).

[25] W. Tornow, N. Czakon, C. Howell, A. Hutcheson, J. Kelley, V. Litvinenko, S. Mikhailov, I. Pinayev, G. Weisel, and H. Witała, Phys. Lett. B **574**, 8 (2003).

[26] E. C. Schreiber, R. S. Canon, B. T. Crowley, C. R. Howell, J. H. Kelley, V. N. Litvinenko, S. O. Nelson, S. H. Park, I. V. Pinayev, R. M. Prior, K. Sabourov, M. Spraker, W. Tornow, Y. Wu, E. A. Wulf, and H. R. Weller, Phys. Rev. C **61**, 061604(R) (2000).

[27] J. Randrup and R. Vogt, Phys. Rev. C **80**, 024601 (2009).

[28] T. England and B. Rider, *Evaluation and Compilation of Fission*, Tech. Rep. LA-UR-94-3106 (Los Alamos National Laboratory, Los Alamos, 1993).

[29] W. Holubarsch, E. Pfeiffer, and F. Gönnenwein, Nucl. Phys. A **171**, 631 (1971).

[30] F. Vivès, F.-J. Hambsch, H. Bax, and S. Oberstedt, Nucl. Phys. A **662**, 63 (2000).

[31] L. W. Fagg and S. S. Hanna, Rev. Mod. Phys. **31**, 711 (1959).

[32] J. M. Mueller, M. W. Ahmed, B. Davis, J. M. Hall, S. S. Henshaw, M. S. Johnson, H. J. Karwowski, D. Markoff, L. S. Myers, B. A. Perdue, S. Stave, J. R. Tompkins, M. J. Tuffley, and H. R. Weller, Phys. Rev. C **85**, 014605 (2012).

[33] T. Langford, C. Bass, E. Beise, H. Breuer, D. Erwin, C. Heimbach, and J. Nico, Nucl. Instrum. Methods Phys. Res., Sect. A **717**, 51 (2013).

[34] T. S. Carman, V. Litveninko, J. Madey, C. Neuman, B. Norum, P. G. O'Shea, N. R. Roberson, C. Y. Scarlett, E. Schreiber, and H. R. Weller, Nucl. Instrum. Methods Phys. Res., Sect. A **378**, 1 (1996).

[35] N. Pacilio, Reactor Noise Analysis in the Time Domain, US-AEC Critical Review Series TID-24512 (1969).

[36] J. Terrell, Phys. Rev. **108**, 783 (1957).

[37] J. H. Hubbell and S. M. Seltzer, Tables of X-ray mass attenuation coefficients and mass energy-absorption coefficients 1 keV to 20 MeV for elements $Z = 1$ to 92 and 48 additional substances of dosimetric interest, NISTIR-5632 (1995).

[38] J. Huizenga and A. Katsanos, Nucl. Phys. A **98**, 614 (1967).

[39] J. T. Caldwell, E. J. Dowdy, R. A. Alvarez, B. L. Berman, and P. Meyer, Nucl. Sci. Eng. (La Grange Park, IL, U. S.) **73**, 153 (1980).

[40] D. Findlay, N. Hawkes, and M. Sené, Nucl. Phys. A **458**, 217 (1986).

[41] M. Chadwick *et al.*, Nucl. Data Sheets **112**, 2887 (2011).

[42] A. Lengyel, O. Parlag, V. Maslyuk, M. Romanyuk, and O. Gritzay, J. Nucl. Part. Phys. **6**, 43 (2016).

[43] N. S. Rabotnov, G. N. Smirenkin, A. S. Soldatov, L. N. Usachev, S. P. Kapitza, and Y. M. Tsipenyu, Sov. J. Nuclear Phys. **11**, 285 (1970).

[44] C. D. Bowman, I. G. Schröder, K. C. Duvall, and C. E. Dick, Phys. Rev. C **17**, 1086 (1978).

[45] V. Zhuchko, Y. B. Ostapenko, G. Smirenkin, A. Soldatov, and Y. M. Tsipenyuk, Sov. J. Nuclear Phys. **28**, 1185 (1978).

[46] J. T. Caldwell, E. J. Dowdy, B. L. Berman, R. A. Alvarez, and P. Meyer, Phys. Rev. C **21**, 1215 (1980).

[47] D. Brown *et al.*, Nucl. Data Sheets **148**, 1 (2018).

[48] J. Knowles, W. Mills, R. King, B. Pich, S. Yen, R. Sobie, L. Watt, T. Drake, L. Cardman, and R. Gulbranson, Phys. Lett. B **116**, 315 (1982).

[49] P. A. Dickey and P. Axel, Phys. Rev. Lett. **35**, 501 (1975).

[50] M. Yester, R. Anderm, and R. Morrison, Nucl. Phys. A **206**, 593 (1973).
[51] O. Mafra, S. Kuniyoshi, and J. Goldemberg, Nucl. Phys. A **186**, 110 (1972).
[52] A. Khan and J. Knowles, Nucl. Phys. A **179**, 333 (1972).
[53] R. Anderl, M. Yester, and R. Morrison, Nucl. Phys. A **212**, 221 (1973).
[54] C. D. Bowman, I. G. Schröder, C. E. Dick, and H. E. Jackson, Phys. Rev. C **12**, 863 (1975).
[55] Y. B. Ostapenko, G. Smirenkin, A. Soldatov, V. Zhuchko, and Y. M. Tsipenyuk, Vop. At. Nauki i Tekhn., Ser. Yadernye Konstanty **3**, 3 (1978).
[56] A. Soldatov and G. Smirenkin, Sov. J. Nuclear Phys. **55**, 1757 (1992).
[57] A. Manfredini, M. Muchnik, L. Fiore, C. Ramorino, H. De Carvalho, R. Bösch, and W. Wölfli, Nuovo Cimento B **44**, 218 (1966).
[58] M. Herman, R. Capote, B. Carlson, P. Obložinský, M. Sin, A. Trkov, H. Wienke, and V. Zerkin, Nucl. Data Sheets **108**, 2655 (2007).
[59] M. W. Ahmed, A. E. Champagne, C. R. Howell, W. M. Snow, R. P. Springer, and Y. Wu, *HIGS2: The Next Generation Compton γ-Ray* (Triangle Universities Nuclear Laboratory, Durham, 2012).